Two cone-beam consistency conditions for a circular trajectory

Jérôme Lesaint, Rolf Clackdoyle, Simon Rit, Laurent Desbat

***Abstract*—Data consistency conditions are equations that should be satisfied by the projection data if the underlying line integral model perfectly matches the physical reality. In this work, we propose two cone-beam consistency conditions based on previous theoretical works. The source trajectory is circular, with the detector oriented perpendicularly to the plane of the trajectory, as usual. The conditions apply equally well to any planar source trajectory. We introduce two DCC functions that are applied to the cone-beam projections, such that the same constant function value occurs for all projections provided the data are consistent. Evaluations of the functions are easily implemented and any projection whose DCC function value deviates from the constant indicates inconsistency with the rest of the data.**

I. Introduction and related work

Characterization of the range of integral operators involved in Computed Tomography (CT) has been studied for decades, from the classical Helgason-Ludwig data consistency conditions (DCCs) [1], [2] for parallel beam geometry to more recent DCCs in fanbeam geometry [3]–[5]. For the 3D cone-beam (CB) geometry, DCCs have been derived in [6]–[9]. Beyond their theoretical interest, DCCs can be used to detect some systematic effects like patient motion [10], [11] or failing equipment [12], to automatically calibrate CT systems [13] or to correct scatter [14]. In this work, we build upon existing CB theory [15], [16] within a common framework [17]–[19] to develop simple DCCs for the standard circular CB geometry and other planar source trajectories.

II. Notation and theoretical background

We consider a CB-CT system made up of an X-ray source and a flat detector, both undergoing a planar source trajectory (typically, a circle) around the object of interest. The plane containing the trajectory is denoted Π_S. The source location is $\vec{a}_\lambda$ parametrized by the angle $\lambda \in \Lambda$ where $\Lambda \subset \mathbb{R}$ is an interval. Throughout the trajectory, the detector plane Π_λ is perpendicular to Π_S. We let $\vec{u}$ denote one of the two possible unit vectors in the direction of the intersection $\Pi_S \cap \Pi_\lambda$ (for example, the one parallel to the motion of the source). *For each projection*, we define a detector reference frame as follows:

J. Lesaint, R. Clackdoyle and L. Desbat are with the TIMC-IMAG laboratory, CNRS UMR 5525 and Université Grenoble Alpes (e-mail : lesainje@imag.fr and laurent.desbat@imag.fr).

S. Rit is with the CREATIS laboratory, CNRS UMR 5520 and INSERM U1044, Lyon, France (e-mail : simon.rit@creatis.insa-lyon.fr).

This work is partially supported by the Agence Nationale de la Recherche (France), Labex CAMI, number ANR-11-LABX-0004-01 and project "DROITE", number ANR-12-BS01-0018.

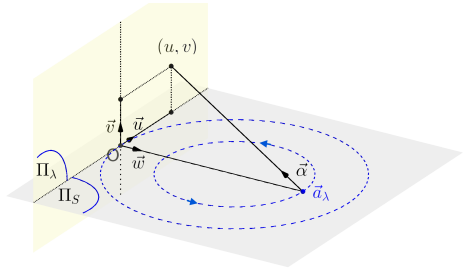

Fig. 1. Description of the geometry and choice of coordinate system. The source $\vec{a}_\lambda$ moves along the circle. And the detector moves accordingly.

the origin is the orthogonal projection of the source onto the detector (the *principal point*). The normal to the detector is $\vec{w}$, pointing in the direction of the source, so that $\vec{a}_\lambda = d\ \vec{w}$ (where d is the distance from the source to the detector). We set $\vec{v}$ so that $(\vec{u}, \vec{v})$ define a reference frame of the detector and $(\vec{u}, \vec{v}, \vec{w})$ is a 3D reference frame. A point on the detector can be written $u\vec{u} + v\vec{v}$. See Fig. 1.

The 3D Radon transform of an attenuation function f is defined by:

$$\mathcal{R}f(\vec{\beta}, s) = \int_{\vec{\beta}^\perp} f(s\vec{\beta} + \vec{y})d\vec{y}$$

with $\vec{\beta} \in \mathbb{S}^2$ ($\mathbb{S}^2$ denotes the unit sphere in $\mathbb{R}^3$) and $s \in \mathbb{R}$. Given a fixed $\vec{\beta} \in \mathbb{S}^2$, we also denote $\mathcal{R}_\beta f$ the 1D-function: $\mathcal{R}_\beta f(s) = \mathcal{R}f(\beta, s)$. The CB projections are defined over the set $\Lambda \times \mathbb{S}^2$ by :

$$g(\lambda, \vec{\alpha}) = \mathcal{D}f(\lambda, \vec{\alpha}) = \int_0^{+\infty} f(\vec{a}_\lambda + t\vec{\alpha})dt \qquad (1)$$

Early CB CT reconstruction methods are based on links between filtering CB data and filtering 3D Radon transform. Following [17] an intermediate function G is defined on the set $\Lambda \times \mathbb{S}^2$ by:

$$G(\lambda, \vec{\beta}) = \int_{\mathbb{S}^2} h(\vec{\alpha} \cdot \vec{\beta})g(\lambda, \vec{\alpha})d\vec{\alpha}, \qquad (2)$$

where the generalized function h is positively homogeneous of degree -2, i.e. $\forall k > 0,\ h(ks) = (1/k^2)h(s)$. In this work, h can be either odd ($\forall x \in \mathbb{R}, h(-x) = -h(x)$) or even ($\forall x \in \mathbb{R}, h(-x) = h(x)$). The relation between the function G and the 3D Radon transform of f is given by:

$$G(\lambda, \vec{\beta}) = s_h \left(h * \mathcal{R}_{\vec{\beta}} f\right)(\vec{a}_\lambda \cdot \vec{\beta}), \qquad (3)$$

where $s_h = 1$ if h is even and -1 if h is odd. A proof of this result can be found in [18]. Note that if the projection data are given by Eq. (1) and if some plane $\Pi(\vec{\beta}, s)$ - defined by its normal direction $\vec{\beta}$ and its signed distance to origin s - contains two source positions $\vec{a}_{\lambda_1}$ and $\vec{a}_{\lambda_2}$ (meaning that $\vec{a}_{\lambda_1} \cdot \vec{\beta} = \vec{a}_{\lambda_2} \cdot \vec{\beta}$), then:

$$G(\lambda_1, \vec{\beta}) = G(\lambda_2, \vec{\beta}). \tag{4}$$

Equation 4 provides a consistency condition.

III. Implementation

In this section, we investigate two practical aspects of the implementation of these DCCs: the evaluation of the function G and the choice of the filter h.

A. Evaluation of the function G

In order to evaluate the function G in practice, we need to express Eq. 2 in terms of detector coordinates. With the (u, v) coordinates of the detector (see Sec. II and Fig. 1), one can write:

$$\vec{\alpha} = \vec{\alpha}(u, v) = \frac{u\vec{u} + v\vec{v} - d\vec{w}}{\sqrt{u^2 + v^2 + d^2}}.$$

This change of variables leads to the following expression:

$$G(\lambda, \vec{\beta}) = s_h \left(h * \mathcal{R}_{\vec{\beta}_D} \tilde{g}_\lambda \right) (\vec{a}_\lambda \cdot \vec{\beta}), \tag{5}$$

where $\tilde{g}$ denotes pre-weighted projections:

$$\tilde{g}_\lambda(u, v) = \tilde{g}(\lambda, u, v) = \frac{d}{\sqrt{u^2 + v^2 + d^2}} g(\lambda, \vec{\alpha}(u, v)).$$

In Eq. 5, $\mathcal{R}\tilde{g}_\lambda$ is the 2D Radon transform at fixed direction $\vec{\beta}_D$ of $\tilde{g}_\lambda$:

$$\mathcal{R}_{\vec{\beta}_D} \tilde{g}_\lambda(s) = \int_{\mathbb{R}} \tilde{g}_\lambda(s\vec{\beta}_D + l\vec{\beta}_D^{\perp}) dl$$

and $\vec{\beta}_D$ denotes the normalized orthogonal projection of $\vec{\beta}$ onto the detector plane Π_λ. As Eq. 5 shows, the evaluation of $G(\lambda, \vec{\beta})$ is three steps : pre-weighting the projection, computation of the 2D Radon transform along lines perpendicular to $\vec{\beta}_D$ and convolution of this 1D function with h at $\vec{a}_\lambda \cdot \vec{\beta}$. While pre-weighting in step 1 is familiar, step 2 may be more involved if $\vec{\beta}_D$ is not aligned with pixel lines and may require complex re-binning and/or backprojection of the data in a virtual detector. The particular choice which is made in this work, makes computations in step 2 considerably easier. This choice is $\vec{\beta} = \vec{v}$. The main result of this work is the following:

Proposition 1. *Let $g = \mathcal{D}f$ for some object function f, with a planar source trajectory $\{\vec{a}_\lambda \in \mathbb{R}^3, \lambda \in \Lambda\} \subset \Pi_S$; Let h be positively homogeneous of degree -2, odd or even ; the function G defined by:*

$$G(\lambda, \vec{v}) = \int_{\mathbb{S}^2} h(\vec{\alpha} \cdot \vec{v}) g(\lambda, \vec{\alpha}) d\vec{\alpha} \tag{6}$$

is constant (independent of λ).

To better understand this statement, we replace $\vec{\beta}$ with $\vec{v}$ in Eq. 5. For all λ, $\vec{a}_\lambda \cdot \vec{v} = 0$ and $\mathcal{R}_{\vec{\beta}_D} \tilde{g}_\lambda$ is $\mathcal{R}_{\vec{v}} \tilde{g}_\lambda$, the 2D Radon transform of the pre-weighted projection *in the direction* $\vec{u}$ (i.e. along pixel lines) thus depending only on v. Let l_λ be this 1D function defined (in the (u, v) coordinates of the detector) by:

$$l_\lambda(v) = \mathcal{R}_{\vec{v}} \tilde{g}_\lambda(v) = \int \tilde{g}_\lambda(u, v) du, \tag{7}$$

Plugging (7) into (5), Eq. (6) now reads:

$$G(\lambda, \vec{v}) = s_h (h * l_\lambda)(0). \tag{8}$$

B. Choice for the function h

The intermediate function G defined in [17] provides with a unifying framework for various early 3D reconstruction formulas such as the ones from Smith [15] and Grangeat [16], [20]. Both approaches correspond to different choices for the function h. Smith's approach is based on the ramp filter:

$$h_R(s) = \int_{\mathbb{R}} |\sigma| e^{2i\pi\sigma s} ds.$$

Grangeat's approach is based on the derivative filter:

$$h_D(s) = \int_{\mathbb{R}} 2i\pi\sigma e^{2i\pi\sigma s} d\sigma.$$

It is easily verified that both h_R and h_D are positively homogeneous of degree -2 and that they are even and odd respectively.

The choice of h will impact the implementation of Eq. (8). In the case $h = h_D$, Eq. (8) reduces to: $-l'_\lambda(0)$, the derivative of l_λ taken at $v = 0$. The function l will only need to be evaluated in a neighbourhood of $v = 0$ in order to estimate this derivative. In the case $h = h_R$, Eq. (8) remains a standard convolution and the function l_λ will have to be evaluated for all possible v (i.e. on all detector lines). h_D is a local filter whereas h_R is global.

IV. Experiments and results

The following experiments aim to demonstrate that the consistency condition claimed in Proposition 1 can detect unwanted systematic effect in the data. Moreover, the ability to choose between two filters provides flexibility in the task under study.

A. Material and methods

We used a standard Shepp-Logan phantom for the simulations, as described in [21]. Projections were computed using the *Reconstruction ToolKit* [22]. The trajectory of the source was a circle with radius 100. 72 projections were computed over a full angular range of 360 degrees ($\lambda \in [0, 2\pi)$). The source-to-detector distance was 200. The exterior ellipsoid of the phantom has axis semi-lengths of $(55.2, 73.6, 72)$. Each projection has 1024×1024 pixels. And the cone angle was $104°$ in both directions. The extremely large cone-angle was intentional, to emphasize the divergent ray effects because the function $l_\lambda(v)$ is the same for all projections in the parallel case and the consistency conditions are then trivial. The detector is assumed to be perfectly aligned so that pixel lines are aligned with the u-coordinate. Hence, no interpolation was necessary to evaluate the function l_λ as described above.

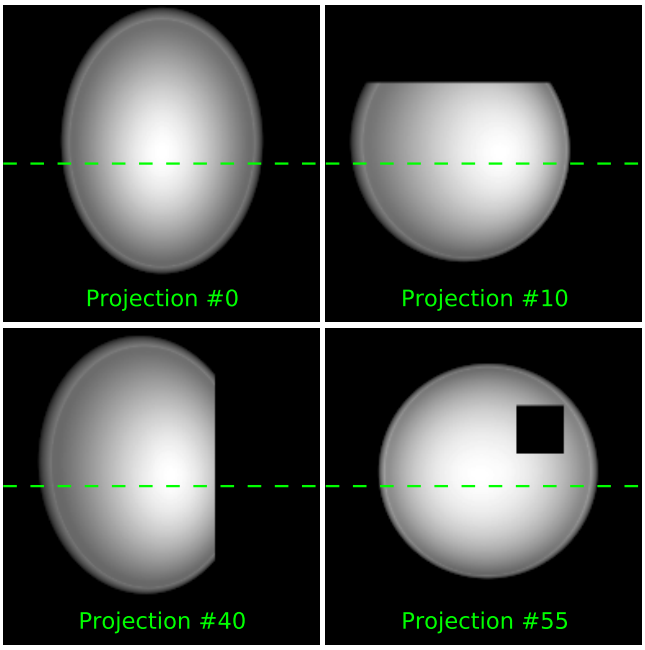

Fig. 2. Scenario 1 : projection truncations. Among the 72 projections, three were truncated as indicated. The dotted line indicates the line $v = 0$. Truncation of proj. #10 (*top right*) is away from the line. Truncation of proj. #40 (*bottom left*) impacts the line. Truncation of proj. #55 (*bottom right*) *is closer to the line. See text for analysis.*)

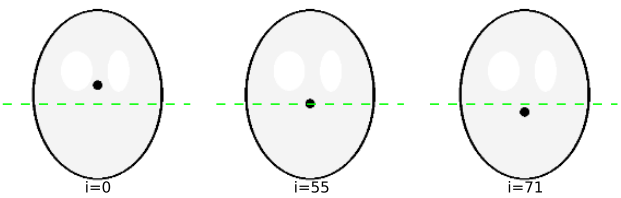

Fig. 3. Scenario 2 : organ motion. The phantom is kept fixed from projections #1 to #20. From projection #21 to the end, one of the ellipsoids is moving. The motion is linear, perpendicular to the line $v = 0$ (dotted line). The moving ellipsoid is a ball of radius 4 and has density 1.0. It intersects the central line in the range of projections #47 to #65.

The derivative filter was implemented with a central difference approximation. The ramp filter was implemented as described in [21]. We also applied a smoothing filter in the v-direction, to account for numerical instabilities. The filter has a support of length 11 pixels. It is applied after the ramp (or derivative) filter.

In the sequel, G_D and G_R denote the function G with the corresponding h_D and h_R respectively. In our first experiment, we study the behaviour of G_R and G_D with respect to truncations. In three projections (#10, 40 and 55), part of the projection is set to zero. Truncation of projection #40 is symmetric around the line $v = 0$ in the detector and simulates a large patient. Truncation of projection #10 is a trans-axial truncation (see Fig. 2). Projection #55 simulates a defect on the detector or an occlusion.

In the second experiment, we simulated an organ motion by moving an ellipsoid along a linear trajectory that crosses the line $v = 0$. The ellipsoid keeps a fixed position during the first 20 projections, then undergoes its motion till the end of acquisition cycle (see Fig. 3).

For each experiment, we compute and plot the function G_D and G_R. And as Proposition 1 states, if the data are consistent, we expect a constant plot.

B. Results

Figure 4 shows the results.

1) Truncation: The use of the ramp filter allows for the detection of any truncation, wherever this truncation occurs whereas only the lateral truncation is detected by the derivative filter (see Fig. 4, *left*). Because the ramp filter has an infinite support, it will detect truncation anywhere in the data (see Fig. 4, *bottom left*). On the other hand, the derivative filter is local and will only detect truncation in the neighbourhood of the line $v = 0$ (see Fig. 4, *top left*). It should be noticed that truncation in projection #10 was detected by the ramp filter because the inconsistency was "massive". It would not be able to detect a lighter modification that was far from the central line. The reason being that the lower response of the DCC would be indistinguishable from the background numerical instability.

2) Motion: For the motion experiment, we observed similar behaviour. The derivative filter detected the motion only when the object crossed the line $v = 0$ (see Fig. 4, *top right*). On the other hand, with the ramp filter (see Fig. 4, *bottom right*), the function G_R deviated from its (approximately) constant value long before the object crossed the line $v = 0$. This, again, reflected the global nature of the ramp filter, which makes the DCC able to detect almost any consistency, almost anywhere in the data.

V. Discussion

In this paper, we have revisited existing theoretical results from the DCC perspective. The necessary consistency conditions we derived are easy to implement, comprehensive in the sense that they scan all the data at once and valid under reasonable assumptions on the acquisition geometry. First numerical experiments demonstrate the potential to use the DCC for the detection of data inconsistencies, e.g. truncation, motion. The interesting point in the above experiments is the complementary role that the two filters h_R and h_D can play in the detection of systematic effects directly from the projection data. The ramp filter is able to detect any inconsistency anywhere in a projection. The ramp filter is global. On the other hand, the derivative filter only detects inconsistencies in the neighbourhood of the central plane. The derivative filter is local. As an example, the derivative filter does not detect truncation not affecting the central plane. Depending on the problem under study, this may be an advantage or a disadvantage (consider the case where motion in the central plane needs to be identified while truncation away from this plane occurs). We also noticed the limits of both filters: one

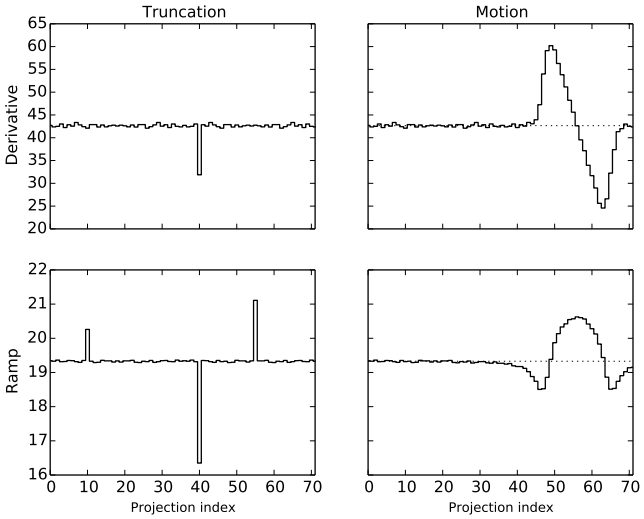

Fig. 4. Numerical simulations : plot of the function G_D (*top*) and G_R (*bottom*) with respect to projection number in the case of truncation (*left*) or motion (*right*). The x-axis is the projection index. The dotted line on the right-hand column is the mean value of the function with no inconsistency.

of them is the numerical instability that prevents detection of low-level inconsistencies far from the central line. The use of a smoothing filter to reduce this noise comes with the attenuation of respective specificities of the two functions.

We emphasize the fact that the DCC with the ramp filter is a truly CB DCC: all the data in each projection are involved in the evaluation of the DCC function. On the other hand, the derivative version is equivalent to a 2D fanbeam DCC: only the data on the intersection of the projection plane with the central plane are used.

Finally, note that we could have considered different $\vec{\beta}$ (not in the $\vec{v}$ direction) in order for the derivative version to access other parts of the projection data. In this case however, the DCC would only be able to compare the projections pairwise (only two cone-beam projections at a time), because for $\vec{\beta}$ different from $\vec{v}$, the plane orthogonal to $\vec{\beta}$ will intersect the source trajectory in at most two points. Whereas, with the specific choice we made for $\vec{\beta}$, all the projections can be checked at once.

References

[1] D. Ludwig, "The radon transform on euclidean space," *Communications on Pure and Applied Mathematics*, vol. 19, no. 1, pp. 49–81, 1966. [Online]. Available: http://dx.doi.org/10.1002/cpa.3160190105

[2] S. Helgason, *The Radon transform*, ser. Progress in mathematics. Boston, Basel, Berlin: Birkhuser, 1999. [Online]. Available: http://opac.inria.fr/record=b1095821

[3] R. Clackdoyle, "Necessary and sufficient consistency conditions for fanbeam projections along a line," *Nuclear Science, IEEE Transactions on*, vol. 60, no. 3, pp. 1560–1569, 2013.

[4] R. Clackdoyle and L. Desbat, "Data consistency conditions for truncated fanbeam and parallel projections," *Medical Physics*, vol. 42, no. 2, pp. 831–845, 2015. [Online]. Available: http://scitation.aip.org/content/aapm/journal/medphys/42/2/10.1118/1.4905161

[5] H. Yu, G. Wang, J. Yang, J. D. Pack, M. Jiang, and B. De Man, "Data consistency condition for truncated projections in fan-beam geometry," *Journal of X-ray science and technology*, vol. 23, no. 5, pp. 627–638, 2015.

[6] F. John, "The ultrahyperbolic differential equation with four independent variables," *Duke Math. J.*, vol. 4, no. 2, pp. 300–322, 06 1938. [Online]. Available: http://dx.doi.org/10.1215/S0012-7094-38-00423-5

[7] S. K. Patch, "Consistency conditions upon 3d ct data and the wave equation," *Physics in Medicine and Biology*, vol. 47, no. 15, p. 2637, 2002. [Online]. Available: http://stacks.iop.org/0031-9155/47/i=15/a=306

[8] M. S. Levine, E. Y. Sidky, and X. Pan, "Consistency conditions for cone-beam ct data acquired with a straight-line source trajectory," *Tsinghua science and technology*, vol. 15, no. 1, pp. 56–61, Feb. 2010. [Online]. Available: http://www.ncbi.nlm.nih.gov/pmc/articles/PMC2886312/

[9] R. Clackdoyle and L. Desbat, "Full data consistency conditions for cone-beam projections with sources on a plane," *Physics in Medicine and Biology*, vol. 58, no. 23, p. 8437, 2013. [Online]. Available: http://stacks.iop.org/0031-9155/58/i=23/a=8437

[10] W. Wein and A. Ladikos, "Towards general motion recovery in cone-beam computed tomography," in *Proceedings of The 12th International Meeting on Fully Three-Dimensional Image Reconstruction in Radiology and Nuclear Medicine*, 2013, pp. 54–57.

[11] R. Frysch and G. Rose, "Rigid motion compensation in interventional c-arm ct using consistency measure on projection data." in *Proceedings of the 18th International Conference on Medical Image Computing and Computer Assisted Interventions*, 2015.

[12] S. Patch, "Moment conditions indirectly improve image quality," *Contemporary Mathematics*, vol. 278, pp. 193–206, 2001.

[13] N. Maass, F. Dennerlein, A. Aichert, and A. Maier, "Geometrical jitter correction in computed tomography," in *Proceedings of the third international conference on image formation in x-ray computed tomography*, F. Noo, Ed., 2014, pp. 338–342.

[14] C. Kim, M. Park, Y. Sung, J. Lee, J. Choi, and S. Cho, "Data consistency-driven scatter kernel optimization for x-ray cone-beam ct," *Physics in Medicine and Biology*, vol. 60, no. 15, p. 5971, 2015. [Online]. Available: http://stacks.iop.org/0031-9155/60/i=15/a=5971

[15] B. Smith, "Image reconstruction from cone-beam projections: Necessary and sufficient conditions and reconstruction methods," *Medical Imaging, IEEE Transactions on*, vol. 4, no. 1, pp. 14–25, March 1985.

[16] P. Grangeat, "Mathematical framework of cone beam 3d reconstruction via the first derivative of the radon transform," in *Mathematical Methods in Tomography*, ser. Lecture Notes in Mathematics, G. Herman, A. Louis, and F. Natterer, Eds. Springer Berlin Heidelberg, 1991, vol. 1497, pp. 66–97. [Online]. Available: http://dx.doi.org/10.1007/BFb0084509

[17] R. Clackdoyle and M. Defrise, "Overview of reconstruction algorithms for exact cone-beam tomography," *Proc. SPIE*, vol. 2299, pp. 230–241, 1994. [Online]. Available: http://dx.doi.org/10.1117/12.179253

[18] R. Clack and M. Defrise, "Cone-beam reconstruction by the use of radon transform intermediate functions," *J. Opt. Soc. Am. A*, vol. 11, no. 2, pp. 580–585, Feb 1994. [Online]. Available: http://josaa.osa.org/abstract.cfm?URI=josaa-11-2-580

[19] F. Noo, "Méthodes numériques directes de reconstruction d'images tridimensionnelles à partir de projections coniques." Ph.D. dissertation, Université de Liège, 1998.

[20] P. Grangeat, "Analyse d'un systeme d'imagerie 3d par reconstruction a partir de radiographies x en geometrie conique," Ph.D. dissertation, 1987, thse de doctorat dirige par GARDERET, PHILIPPE Sciences appliques ENST 1987. [Online]. Available: http://www.theses.fr/1987ENST0011

[21] A. Kak and M. Slaney, *Principles of Computerized Tomographic Imaging*. Society for Industrial and Applied Mathematics, 2001. [Online]. Available: http://epubs.siam.org/doi/abs/10.1137/1.9780898719277

[22] S. Rit, M. V. Oliva, S. Brousmiche, R. Labarbe, D. Sarrut, and G. C. Sharp, "The reconstruction toolkit (rtk), an open-source cone-beam ct reconstruction toolkit based on the insight toolkit (itk)," *Journal of Physics: Conference Series*, vol. 489, no. 1, p. 012079, 2014. [Online]. Available: http://stacks.iop.org/1742-6596/489/i=1/a=012079